



Mesoscopic model framework for liquid slip in a confined parallel-plate flow channel

Zi Li ^{1,2,*}, Jiawei Li,³ Guanxi Yan,² Sergio Galindo-Torres,¹
Alexander Scheuermann ² and Ling Li¹

¹*Institute of Advanced Technology, Westlake Institute for Advanced Study, Hangzhou 310024, China
and Key Laboratory of Coastal Environment and Resources of Zhejiang Province,*

School of Engineering, Westlake University, Hangzhou 310024, China

²*School of Civil Engineering, The University of Queensland, Brisbane 4072, Australia*

³*Key Laboratory for Thermal Science and Power Engineering of Ministry of Education, Department of
Energy, and Power Engineering, Tsinghua University, Beijing 100084, China*



(Received 29 June 2020; accepted 2 March 2021; published 22 March 2021)

Liquid slip significantly affects confined fluid flow. The physical origin of slip flow with the Knudsen number ranging from 0.001 to 0.1 can be attributed to the long-range intermolecular fluid-solid interaction (FSI) force. To this end, in the framework of the mesoscopic lattice Boltzmann model (LBM), an exponentially decaying force function between fluid particles and two confined flat walls is proposed herein. For the parallel walls of symmetric FSI forces, we explicitly link density profile, velocity profile, apparent slip length, and permeability-enhancement ratio with the mesoscale FSI parameters (strength and decay length); by nondimensionalization of the exact solutions, we also acquire two dimensionless numbers that indicate the role of complex FSI strength and gap size of the flow channel in the slip-flow system. For the walls with asymmetric FSI properties, the numerical profiles of density and velocity as well as the amount of slip can be provided by the LBM simulations. The curve for continuous FSI force with two free parameters is calibrated for the hydrophobic surfaces in two benchmark flow experiments. Results show that the proposed FSI force function provides a robust model framework to mesoscopically elucidate the physical process of liquid slip flow.

DOI: [10.1103/PhysRevFluids.6.034203](https://doi.org/10.1103/PhysRevFluids.6.034203)

I. INTRODUCTION

The fluid slip at the solid surface usually plays an unnoticeable role in macroscale flows, but it can be dominant in confined flow channels at the micro- or nanoscale [1]. The flow regimes of confined fluid flow can be characterized by the Knudsen (Kn) number, a ratio of the molecular mean free path to the representative length of the flow channel [2,3]. As Kn number increases, the intermolecular collision and attraction between fluid molecules and solid wall become increasingly significant relative to those between fluid molecules themselves, and the continuum regime ($\text{Kn} < 0.001$) tends to transit to the slip regime ($0.001 < \text{Kn} < 0.1$), transitional regime ($0.1 < \text{Kn} < 10$), and molecular free regime ($\text{Kn} > 10$) [2,3]. This paper focuses on the liquid flow in the slip regime, often encountered in the transport of water in tight sandstone and of oil in shale matrix, where the continuum and thermodynamic equilibrium assumptions still hold in the bulk fluid, but it is necessary that a slip boundary condition be introduced.

*lizi@westlake.edu.cn

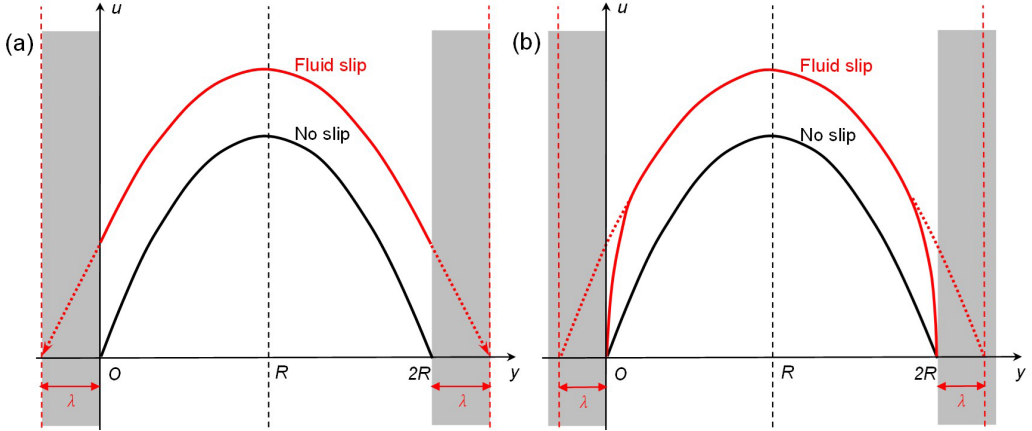


FIG. 1. Diagram of velocity profile and ASL for the cases of true slip (a) and apparent slip (b) in a confined parallel-plate flow channel with a gap of $2R$.

One variable for quantifying the amount of fluid slip is the permeability-enhancement ratio (PER, k_{ra}) in terms of volumetric or mass flux, viz., the ratio of flux (Q_s) in the slip flow to flux (Q_{ns}) with a no-slip boundary condition satisfied, $k_{ra} = Q_s/Q_{ns}$, with the same diameter of the flow channel and the same pressure gradient applied but different surface chemical properties of the solid wall. The other variable is slip length (λ) in a length scale, defined as the distance between the real solid wall and the fictitious solid wall, where the bulk velocity (u) extrapolates to zero tangentially [see Fig. 1(a)] or remains a Poiseuille-flow fashion [see Fig. 1(b)], as given by

$$u|_{y=0} = \lambda \left. \frac{\partial u}{\partial y} \right|_{y=0}, \quad (1)$$

$$u = \frac{(-\nabla p + \rho g)}{2\mu} (y + \lambda)(2R + \lambda - y), \quad (2)$$

with y being the axis normal to the solid wall, $(-\nabla p + \rho g)$ being the sum of pressure and gravitational gradients imposed on the fluid, and μ being bulk fluid viscosity. The first case is referred to as true slip because fluid molecules are directly sliding on solid walls, due to the motion of near-wall fluid molecules under the rarefied condition [4,5]. Actually, Eq. (1) was initially raised to modify the no-slip boundary condition as one of Navier's pioneering works. Since then it has been being applied to the slip flow in the slip regime. Instead, apparent slip in the second case occurs on the fluid-fluid interface due to the varying viscosity of near-wall liquid as a result of the long-range intermolecular fluid-wall interaction [4,5]. This effective approach simplifies the hydrodynamic analysis by taking the mesoscopically induced low interfacial friction into consideration. In this work, apparent slip length (ASL) as defined in Eq. (2), which is responsible for the increased permeability of flow channel in the slip regime of our interest, will be used for analysis. Because it can be positive or negative depending on the surface chemical property of the solid wall, and also it is geometrically meaningful in that the slip-flow system behaves as if the effective gap between the two flat walls increases by double ASLs.

The enhanced flow rate in thin capillaries [6,7] and the slip velocity profile in hydrophobic microchannel flows [8,9] have been observed by laboratory measurements. The value of PER for thin channels with a diameter of 1 micron (μm) reaches approximately 1.30 [7]. The ASL values of typical and engineered hydrophobic surfaces range from 1 to 100 nanometers (nm) [1] to around 1 μm [8]. The apparent fluid slip should be therefore carefully considered when estimating the transport properties of a liquid in tight porous media. Sometimes the adsorbed liquid layer and lower

than expected water flow [10,11] can also be observed in low-permeability reservoirs. Apparent slip flow occurs over a boundary layer with a large velocity gradient. This film layer is proposed to be dissolved gas or a depleted water region [4,5]. Such arguments are supported by the microbubbles observed near hydrophobic surfaces [12]. Flow models considering the thickness of the depleted water region or air gap [13] have been established which, however, cannot reflect the microscopic details of fluid molecules.

At the molecular level, when the long-range liquid-wall attraction becomes much weaker than that between liquid molecules themselves, the liquid cannot fully wet the solid wall and then slip flow occurs over the solid surface. Thus, compared with contact angle, the intermolecular fluid-solid interaction (FSI) force is a more intrinsic variable for descriptions of hydrophobicity of the solid surface. Besides, it recognizes the existence of an adsorbed liquid layer leading to negative ASLs [14], and the fact that liquid can slip on hydrophilic surfaces [15]. The long-range attraction force between liquid molecules and a solid wall is a sum of van der Waals and electrostatic forces [4,5], but it has been just formulated in terms of van der Waals and electrostatic forces individually [16]. Fortunately, its magnitude can be determined in surface force observation systems by the difference between hydrodynamic force on the hydrophilic surface as a no-slip boundary and on the hydrophobic surface with a slip flow [17,18], or by the total hydrodynamic force minus the van der Waals attraction, hydrophobic attraction, and Reynolds drag [19,20].

The intermolecular FSI is quantified in a molecular dynamics simulation by using the Lennard-Jones potential with tunable interaction energies and molecular diameters [21,22], while it is modeled in the lattice Boltzmann method (LBM) by an interaction potential within a single lattice layer [23,24] or by a continuous, monotonic but decaying interaction force [25–31]. The LBM approach assumes no true slip and specifies the FSI strength on the solid surface to result in apparent fluid slip behavior. The continuous force can be established between fluid particles and flat walls. In particular, the Langevin-like frictional force-based LBM [29,30] accounting for graphene oxide–water hydrogen bonding interaction can model water permeability through a graphene oxide membrane; the particle-level force function [31] is capable of investigating the liquid slip flow in porous media. Other LBM models were used to study the gaseous slip on solid surfaces by combining the bounce back and specular reflection boundary conditions [32,33], linking the LBM relaxation time with the Kn number [34,35] or using empirical constitutive relationships between slip velocity and Kn number [36,37].

The mesoscopic LBM model based on gas kinetic theory has been widely used for simulations of slip flow [23–37] and immiscible two-phase flow [38,39]. It is beneficial to the slip-flow simulation, since it not only considers the mesoscopic physics of FSI but also allows simulating the microfluidic flow with moderate computational costs. Therefore, the present study aims to exploit the LBM model framework to investigate the liquid slip flow between two confined parallel plates, which is of crucial importance to estimations of permeability of water in clay material and of oil in shale matrix. Because the local planar flow channels are dominant in clayey soil [40] packed with platy particles, and the use of parallel-plate geometry is well supported in the slit pore of shale fracture with a large length to aperture ratio. Due to the same long-range intermolecular nature [4,5], by an analogy with the hydrophobic attraction between solid surfaces, we propose to describe the physics of fluids near a solid surface by using an exponentially decaying force function [19,20] between fluid particles and two flat walls. Based on this continuous force function, we analytically relate the macroscopic ASL and PER to the mesoscopic interaction physics by deriving the exact solutions for the proposed FSI forces of the two walls.

II. MESOSCOPIC MODEL FRAMEWORK

A. Proposed mesoscopic FSI force function

Near the solid surface, the fluid molecules are subjected to the van der Waals attractions from the fluid molecules in the bulk fluid and from the solid molecules on the wall [16]. Relying on the

difference between the magnitudes of these two attractions, the net force acting on the near-wall fluid molecule, referred to as the apparent extra van der Waals interaction, can be attractive or repulsive. The long-range electrostatic forces are also involved in some more complex systems, such as water flow in clay, where the surface charged clay producing a local electric field can adsorb the polarized water molecules [16]. In this work, the FSI force comprising apparent extra van der Waals and electrostatic components is proposed to result in the negative or positive ASL [4,5]. That our proposed model framework is mesoscopic mainly comes from two aspects: First, each lattice node (particle) in the LBM model represents an assembly of fluid or solid molecules, and the summation of pairwise van der Waals and electrostatic forces between molecules leads to the particle-level FSI force which decays much slower than the molecule-level one spanning only a few molecular spacings [16]; second, regardless of the details of the FSI components, we pay attention to only the total FSI force directly responsible for the apparent slip, which can be measured in surface force apparatus experiments [17–20].

The magnitude of FSI force can be determined in surface force observation systems by the difference between hydrodynamic force on the hydrophilic surface as a no-slip boundary and on the hydrophobic surface with a slip flow [17,18], which shows a continuous, monotonic, and rapidly decaying curve with respect to the distance from the solid surface. The formulation of the FSI force function remains unavailable, but it can be deduced by an analogy with the exponentially decaying hydrophobic attraction force between solid surfaces [19,20], if recognizing that they both have the same intermolecular force components and the same long-range and particle-level nature [31]. In this connection, the decaying nature of an exponential function for the local FSI force can be sustained in the total FSI force after integration over the entire solid wall. Thus, for a confined parallel-plate flow channel, we assume the asymmetric FSI property of the two flat walls and propose an exponential function of the FSI forces $f_{s1} (\neq f_{s2})$ between the fluid particles and the left (right) wall:

$$f_{s1}(y) = \rho(y)g_{s1}\exp\left(-\frac{y}{\eta_1}\right), \quad f_{s2}(y) = -\rho(y)g_{s2}\exp\left(-\frac{2R-y}{\eta_2}\right), \quad (3)$$

where $\rho(y)$ is the transverse density profile in the y direction, $g_{s1} (\neq g_{s2})$ is the interaction strength determining the magnitude of the interaction force, and $\eta_1 (\neq \eta_2)$ is the decay length in a length scale controlling the decaying process of the force curve. Because the directions of the FSI forces from two parallel walls are opposite, they are assigned opposite signs as given by Eq. (3). In order to capture the profiles of density and velocity over the entire flow channel, the formulation of FSI force exerted by the other wall should be considered simultaneously. Then the total interaction force from the two flat walls separated by a gap of $2R$ can be expressed by

$$F_s(y) = \rho(y) \left[g_{s1}\exp\left(-\frac{y}{\eta_1}\right) - g_{s2}\exp\left(-\frac{2R-y}{\eta_2}\right) \right]. \quad (4)$$

The decay profiles of the force curves are shown in Fig. 2(a). The magnitude of the total interaction force reaches a maximum near the solid surface and decays to zero somewhere near the middle of the channel, where the individual interaction forces from the two flat walls are entirely offset. On one hand, the total FSI force is attractive for $g_{s1}(g_{s2}) < 0$. This case features the strong wettability, occurring when the fluid-wall van der Waals attraction is larger than that between fluid molecules [22], and the surface charged solid grain adsorbs the polarized liquid molecule [10]. On the other hand, the total FSI force is repulsive for $g_{s1}(g_{s2}) > 0$ reflecting the hydrophobicity of the solid surface. It may arise when the fluid-wall van der Waals attraction is much weaker than that between fluid molecules [22], and the solid surface is repellent to the nonpolar liquid molecule [11]. The total FSI force decays slower for larger values of η , and the maximum interaction range can reach 20–200 nm [17–20] due to the long-range nature. It is readily accepted that both the larger value of $|g_{s1}|$ ($|g_{s2}|$) and the slower decaying process may indicate a stronger FSI. The proposed FSI force applied to the fluid particles is related to the number density of the fluid particles. In this way,

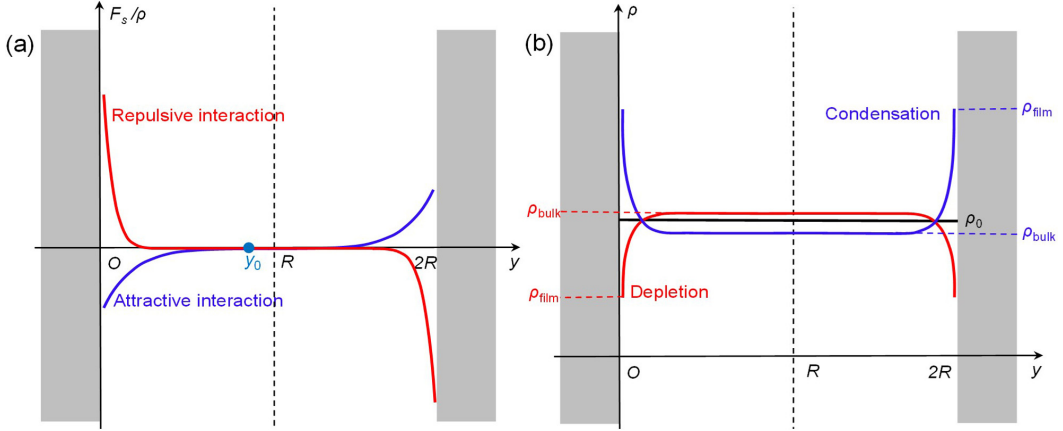


FIG. 2. (a) Diagram of asymmetric force curve ($g_{s1} \neq g_{s2}$, $\eta_1 \neq \eta_2$) for the repulsive or attractive total FSI force. $y = y_0$ is the location where the total FSI force $F_s(y_0) = 0$. (b) Diagram of density profile with a depletion or condensation layer with the film and bulk liquid densities.

the FSI force can change fluid density, dynamic viscosity, and then velocity profile near the solid wall.

The excessive pressure due to the proposed FSI potential plus the ideal gas pressure contributes to the fluid pressure (p), as formulated by Eq. (A3) ([27,28]; see Appendix A). Substituting Eq. (4) into Eq. (A3) gives the explicit formulations for fluid pressure considering the FSI force function:

$$p(y) = \rho(y)R_gT - \int_{y_0}^y \rho(s) \left[g_{s1} \exp\left(-\frac{s}{\eta_1}\right) - g_{s2} \exp\left(-\frac{2R-s}{\eta_2}\right) \right] ds. \quad (5)$$

It is necessary to stress that only the case that the FSI force is dominated by one solid wall which is closer to the fluid particle is considered in our model, because an extreme case would occur if the interaction range of individual FSI force is comparable to the gap size of the flow channel. The net interaction force will become weak due to the offset of the FSI force from the other wall, even if the individual FSI force is strong. This extreme case is characterized by a high Kn number ($\text{Kn} > 0.1$), where the thermodynamic equilibrium does not hold. It can lead to a counterintuitive fact that the slip-flow effect diminishes as the gap between the two walls narrows, and thus our mesoscopic LBM model fails.

It should also be noted here that it is the short-range hydrogen-bonding interaction that induces an epitaxial ordering of only a few monolayers of near-wall liquid molecules, generating a solidlike and locked liquid film which contributes to the no-slip boundary condition. The role of this short-range FSI force has been artificially achieved in our model framework by the use of the bounce-back boundary condition. The wetting solid wall with an attractive FSI property tends to adsorb more fluid particles, and the density of the fluid in the vicinity of the solid wall becomes a bit higher than that of bulk fluid, referred to as the condensation effect [see Fig. 2(b)]. The thickness of the condensation layer (independent of the short-range hydrogen-bonding interaction) can increase to more than several monolayers due to the increased strength of the long-range FSI force, and the adsorbed liquid film stays immobilized at the solid wall, which is named multilayer sticking [22]. For the hydrophobic solid wall of a repulsive FSI property, the near-wall fluid particles can be expelled towards the bulk region, forming a depletion layer near the solid surface with a density lower than that of bulk liquid [see Fig. 2(b)]. In addition to the depletion layer, the other film types characterized by a lighter density of near-wall fluid may include the dissolved gas [4,5], the microbubble coated on the rough solid surface [12], and air gap [13]. Our proposed repulsive FSI model may provide an artificial means of introducing a lower interfacial resistance. The difference

TABLE I. Range of density ratio observed in various experimental investigations.

Reference	Liquid	Solid material	ρ_{ra} range
[41]	Water	Bentonite clay	0.97–0.98
[42]	Water	Kaolinite	0.99–1.68
		Montmorillonite	1.02–1.41
[43]	Water	Glukhovtes kaolin	1.1–1.5
		Cherkassy bentonite	1.1–1.8
[44]	Water	Natural kaolinite	0.98–1.22
		Natural montmorillonite	1.06–1.15
[45]	Water	Silica gel	0.54–1.03
[46]	Water	Cellulose	0.2–1.3

in the density between the film fluid and the bulk liquid has been observed on the surface of clay materials [41–44], silica gel [45], and hydrophilic polymers [46]. The ratio (ρ_{ra}) of film liquid density (ρ_{film}) to bulk liquid density (ρ_{bulk}) is $\rho_{ra} = \rho_{film}/\rho_{bulk}$, where the value maintains around $0.1 < \rho_{ra} < 2.0$ as summarized in Table I.

With the kinematic viscosity independent of the FSI force [31], the dynamic viscosity is proportional to the fluid density. Thus, the depletion (condensation) of liquid film leads to a reduction (increase) of dynamic viscosity and viscous resistance near the solid surface. Accordingly, the flow in the bulk region becomes faster (slower) than that predicted by the no-slip condition with the velocity of near-wall flow still vanishing at the solid wall, and the fictitious no-slip plane lies outside (inside) the flow channel [see Fig. 1(b)], which is the so-called apparent fluid slip (multilayer sticking) behavior. In this way, the proposed repulsive (attractive) FSI force applied to the fluid particles is related to the enhancement (reduction) of flow capability.

B. Lattice Boltzmann governing equation

The intermolecular interaction between liquid molecules in the interior of bulk fluid is assumed to be negligible relative to the intermolecular FSI, because the attraction forces from the neighboring liquid molecules can be counteracted for each bulk liquid molecule. Therefore the stable bulk fluid in a thermodynamic sense can be described by the single-phase LBM model. The particle distribution functions (f_k) in the k th direction of discrete velocity obeys the Bhatnagar-Gross-Krook (BGK) lattice Boltzmann equation [47],

$$f_k(\mathbf{x} + \mathbf{e}_k \Delta t, t + \Delta t) - f_k(\mathbf{x}, t) = \frac{\Delta t}{\tau} [f_k^{eq}(\mathbf{x}, t) - f_k(\mathbf{x}, t)], \quad (6)$$

where \mathbf{x} , t are position and time, respectively; Δt is the time step (ts); \mathbf{e}_k is the discrete velocity; and $f_k^{eq}(\mathbf{x}, t)$ is the Maxwell-Boltzmann equilibrium distribution. The relaxation time (τ) is related to the kinematic viscosity (ν) by $\nu = c_s^2 \Delta t (\tau / \Delta t - 0.5)$, where the speed of sound $c_s = \sqrt{R_g T}$ is fixed at $\sqrt{1/3}$ lu/ts (where lu is the length unit) in this isothermal LBM framework, with R_g and T being the gas constant and Kelvin temperature. The left- and right-hand sides of Eq. (6) are, respectively, the streaming process passing the particle distribution to the neighboring nodes, and the BGK collision operator partially relaxing the particle distribution to the equilibrium distribution.

The explicit force scheme (EFS) is used to quantify the momentum transfer when the total external force (\mathbf{F}) is involved. The forcing term (φ_k), which accounts for changes in the distribution function, and the transformation function (h_k) are defined as [48]

$$\varphi_k(\mathbf{x}, t) = \frac{\mathbf{F} \cdot (\mathbf{e}_k - \mathbf{u}^{eq})}{\rho c_s^2} f_k^{eq}(\mathbf{x}, t), \quad h_k(\mathbf{x}, t) = f_k(\mathbf{x}, t) - \frac{\Delta t}{2} \varphi_k(\mathbf{x}, t), \quad (7)$$

where ρ is the macroscopic fluid density, and \mathbf{u}^{eq} is the equilibrium velocity equal to the macroscopic flow velocity \mathbf{u} . By directly incorporating φ_k into the lattice Boltzmann equation (6) with the collision operator unchanged, and applying h_k to the resulting implicit formula, we obtain the following explicit expression where h_k acts as a new particle distribution function:

$$h_k(\mathbf{x} + \mathbf{e}_k \Delta t, t + \Delta t) - h_k(\mathbf{x}, t) = \frac{1}{\tau} \left[f_k^{\text{eq}}(\mathbf{x}, t) - h_k(\mathbf{x}, t) - \frac{\Delta t}{2} \varphi_k(\mathbf{x}, t) \right] + \Delta t \varphi_k(\mathbf{x}, t). \quad (8)$$

Then the fluid density (ρ) and the flow velocity (\mathbf{u}) are given by

$$\rho = \sum_k h_k, \quad \mathbf{u} = \frac{1}{\rho} \left(\sum_k h_k \mathbf{e}_k + \frac{\Delta t}{2} \mathbf{F} \right). \quad (9)$$

With the gravitational force ($\rho \mathbf{g}$) driving the liquid flow, the total external force applied to the fluid particle can be written as $\mathbf{F} = \mathbf{F}_s + \rho \mathbf{g}$, where \mathbf{F}_s is the long-range FSI force of our interest in Eq. (4) exerted by the solid walls to result in the change of fluid density near the solid surface. The EFS-LBM scheme in Eqs. (6)–(9) can provide the numerical solutions of density and velocity as well as the variables associated with the amount of slip, no matter whether the FSI forces of the two walls are symmetric or asymmetric. Also, it can greatly inhibit the undesirable spurious velocities as a result of the FSI potential used and alleviate the dependence of numerical results on the value of relaxation time. The LBM simulations of a steady-state flow run iteratively before reaching the equilibrium criterion for flow velocity.

C. Navier-Stokes governing equation

In the hydrodynamic limit ($\text{Kn} < 0.1$), the lattice Boltzmann equation (6) can be reduced by using Chapman-Enskog expansion [27,28] to the Navier-Stokes equation for the continuum and slip regimes:

$$\partial_t(\rho \mathbf{u}) + \nabla \cdot \rho \mathbf{u} \mathbf{u} = -\nabla p + \rho \mathbf{g} + \nu \nabla \cdot [\rho(\nabla \mathbf{u} + (\nabla \mathbf{u})^T)], \quad (10a)$$

$$\partial_t \rho + \nabla \cdot (\rho \mathbf{u}) = 0, \quad (10b)$$

When the liquid flow reaches the steady state and maintains a laminar regime, then $\partial_t \rho = 0$, $\partial_t(\rho \mathbf{u}) = 0$, and the inertial term in the momentum balance equation can be neglected. The transverse flow is stagnant, but the fluid density may vary with the distance from the solid wall due to the FSI force. No external body force is present and only the pressure gradient term remains. Thus, Eq. (10a) in the y direction can be rewritten as

$$\partial_y p(y) = 0. \quad (11)$$

For a flow channel with homogeneous gap size, the flow velocity and the fluid density remain constant in the longitudinal direction. No pressure gradient exists and only an external body force is applied. Thus, Eq. (10a) in the x direction reduces to

$$\rho(y)g + \nu \partial_y [\rho(y) \partial_y u(y)] = 0. \quad (12)$$

If assuming the symmetry of the FSI properties of the two walls ($g_{s1} = g_{s2} = g_s$, $\eta_1 = \eta_2 = \eta$), the maximum velocity occurs in the middle of the gap, that is, $y_0 = R$, around which the resulting density profile will show the symmetry. In this case, integration of Eq. (10b) over half of the gap leads to $\partial_t [\int_0^R \rho(y) dy] = 0$, which means that $\int_0^R \rho(y) dy$ remains conservative over time. With the initially specified homogeneous fluid density ρ_0 , the mass balance equation can be written as

$$\int_0^R \rho(y) dy = \rho_0 R. \quad (13)$$

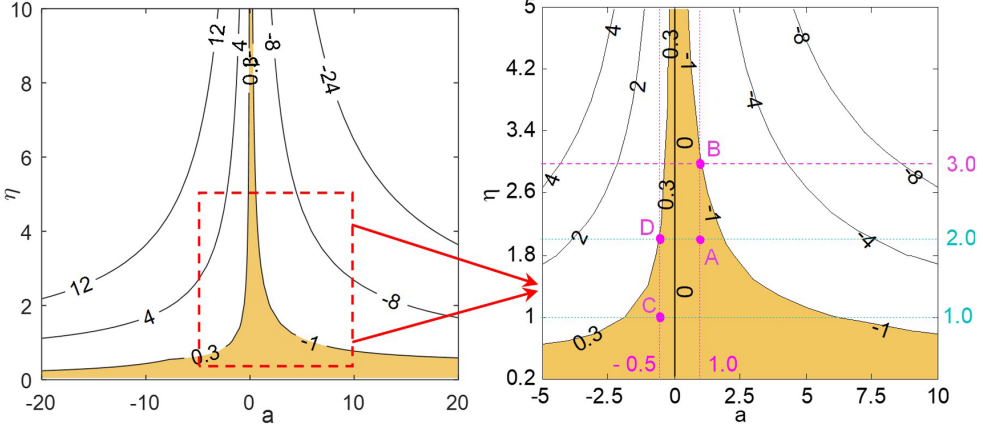


FIG. 3. Profile of density ratio as labeled by the values of $\log_{10}(\rho_{ra})$ with respect to the FSI parameters (a , η). The right panel is an enlarged version of the inset in the left panel as enclosed by the red dashed rectangle. Four pink solid circles (A–D) within the yellow shaded region show the values of (a , η) selected for comparison between analytical solutions and LBM solutions in this subsection. The values of ρ_{ra} for (a , η) at A–D are 0.297, 0.117, 1.202, and 1.834, respectively. $\eta = 1.0$, 2.0 as presented by the two cyan dashed lines are used for investigations of analytical solutions of PER that depend on a in the next subsection. All the variables are presented in lattice units (the same holds in the following figures unless stated otherwise).

Besides, the no-slip boundary condition at $y = 0$ and the maximum velocity at $y_0 = R$ within the gap can both be applied,

$$u(0) = 0, \quad \partial_y u(R) = 0. \quad (14)$$

Then the exact solutions for density profile, velocity profile, and PER, and the asymptotic solution for ASL, can be derived from the governing equations (10) and the auxiliary conditions (11)–(14), as formulated in Eqs. (B3), (B5), and (C7)–(C9) [see Appendixes B and C]. These exact solutions are derived based on the fluid pressure equation (5) with the FSI force function included. They explicitly link the density and velocity profiles, normalized ASL, and volumetric and mass PERs with the mesoscale FSI parameters and the gap size of the flow channel, and they are numerically solvable by using MATLAB in spite of containing single, double, and triple integrals.

Nondimensionalization of these solutions can lead to the dimensionless numbers for the slip-flow system [see Appendix D], such as $[g_s \eta / (R_g T)$, $\eta / R]$, that solely determine the nondimensional density and velocity profiles, normalized ASL, and volumetric and mass PERs, as formulated in Eqs. (D1)–(D5). $g_s \eta / (R_g T)$ provides a complex variable for describing the FSI strength, while η / R represents the FSI range near the solid surface. Large g_s , large η , and small R (i.e., a thin channel) can indicate a strong effect of FSI. Although $R_g T$ in Eq. (5) is fixed at $1/3$ in this isothermal LBM framework, it can be used to measure the compressibility of the working fluid. The fluid is more compressible for a higher value of $1/(R_g T) = \Delta \rho / \Delta p$, and the larger density gradient due to the FSI may result in a more significant slip-flow effect.

III. RESULTS AND ANALYSIS

A. Validation of density and velocity profiles within attainable range of FSI parameters

Each of the exact solutions derived based on the proposed FSI force function has two free parameters. Figure 3 shows the density ratio with respect to these parameters for the gap size of $2R = 200$ lu. In our exact solutions, the film and bulk fluid densities are represented by the fluid

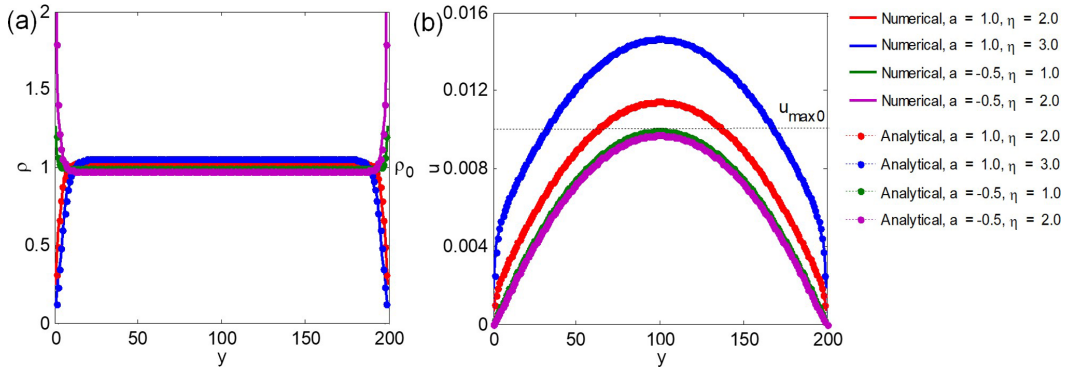


FIG. 4. Comparison of numerical (solid lines) and analytical (dotted dashed lines) solutions for density profile (a) and velocity profile (b). ρ_0 is the initially specified homogeneous fluid density. $u_{\max 0}$ is the maximum velocity in the middle of the gap under the no-slip boundary condition.

densities at the first lattice layer (closest to the solid surface in the lattice grid system) and in the middle of the gap, respectively. The density ratio can reach as high as 10^4 and as low as 10^{-8} .

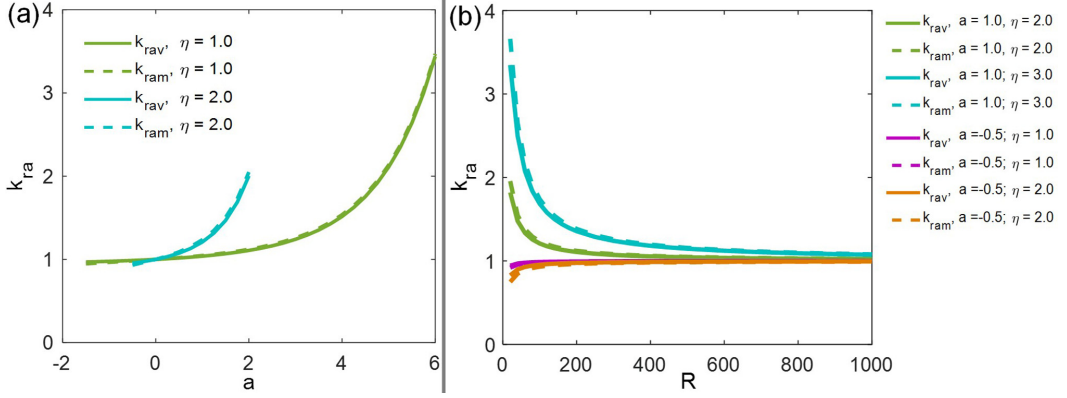
For a higher $|a|$, as defined by $a = g_s/(R_g T)$, or a larger η , which indicates a stronger interaction and a longer interaction range, the density ratios depart further from unity, implying a more intensive depletion (or condensation) effect. However, the range of (a, η) is not arbitrary and should be physically consistent with the observed density ratio [41–46]. The attainable range of (a, η) for the proposed FSI force function is demonstrated by the brown shaded region in Fig. 3, where $0.1 < \rho_{ra} < 2.0$ is satisfied. Following this rule of thumb, the attainable range of a becomes very limited for large η , such as, $\eta > 5$, but very broad for small η . For example, almost all values of a satisfy the specified range of density ratio for fluid slip (multilayer sticking) for $\eta < 0.6$ ($\eta < 0.2$).

Figures 4(a) and 4(b) plot the analytical solutions for density and velocity using the values of (a, η) taken from the shaded range in Fig. 3. For the same $|a|$ but a larger η , the film and bulk fluid densities stay further away from the initially specified density, and the maximum velocities deviate more significantly from that in the no-slip flow. The analytical solutions based on the proposed FSI force function are in excellent agreement with the numerical solutions using the EFS-LBM scheme, validating the accuracy of the analytical solutions numerically solved by MATLAB. These analytical solutions can therefore provide benchmark solutions of liquid slip flow for various advanced LBM schemes and experimental investigations.

B. Relationships of PER with FSI strength, gap size, and dimensionless numbers

The value of PER is usually used in hydrogeology and petroleum engineering to quantify the degree of liquid slip flow through tight sandstone reservoir and shale matrix, which is controlled by the surface chemical property of the solid wall and the size of the gap of the flow channel. Within the attainable range of $|a|$ for $\eta = 1.0, 2.0$ shown in Fig. 3, the volumetric and mass PERs increase superlinearly with a [see Fig. 5(a)] for the gap size of $2R = 200$ lu. In addition, the curves for volumetric and mass PERs are steeper for $\eta = 2.0$ than those for $\eta = 1.0$, implying a more significant FSI effect on the flow properties. The analytical volumetric and mass PERs based on the proposed force function can cover the measured range of PER [3,4]. The curves for the volumetric and mass PERs almost collapse, manifesting the intrinsic behavior of film and bulk fluid density for the proposed force function.

The volumetric and mass PERs increase (decrease) nonlinearly as the gap of the planar channel decreases for $a > 0$ ($a < 0$) [see Fig. 5(b)], which is consistent with the observation that the FSI effect (liquid slip flow) is of great significance in tight porous media. The difference between the volumetric and mass PERs is slight. Also, the PERs converge rapidly to unity as the gap increases.


 FIG. 5. PERs as a function of a (a), and as a function of R (b).

These results indicate the nature of the profiles of fluid density and flow velocity for the proposed force function.

The volumetric PER can be correlated with the ASL directly at the macroscale. Neglecting the effect of near-wall flow on the volumetric flux, we can estimate the volumetric PER by using the approximate bulk velocity profile in Eq. (2) as follows [31]:

$$k_{rav} \approx \begin{cases} 1 + 3\left(\frac{\lambda}{R} + \frac{\lambda^2}{2R^2}\right), & \lambda > 0, \\ \left(1 + \frac{\lambda}{R}\right)^3, & \lambda \leq 0. \end{cases} \quad (15)$$

Figure 6 shows that the estimated volumetric PER from Eq. (15), as a positive correlation with the normalized ASL, agrees well with the exact volumetric PER from Eq. (C8).

Equations (D4) and (D5) provide an exact but complicated function of the two dimensionless numbers. We thus propose a simple exponential relationship:

$$k_{ra} = \exp[\theta_0(a\eta)^{\theta_1}(\eta/R)^{\theta_2}], \quad (16)$$

where θ_0 , θ_1 , and θ_2 are unknown coefficients that can be determined by fitting, and the value of k_{ra} approaches unity if a or η is zero, which recovers the no-slip flow. The value of θ_0 as an intrinsic variable reflects the geometry of the flow channel of the slip-flow system. θ_1 represents the degree of importance of the complex FSI strength $a\eta$ to PER, while θ_2 shows how much the gap size R of

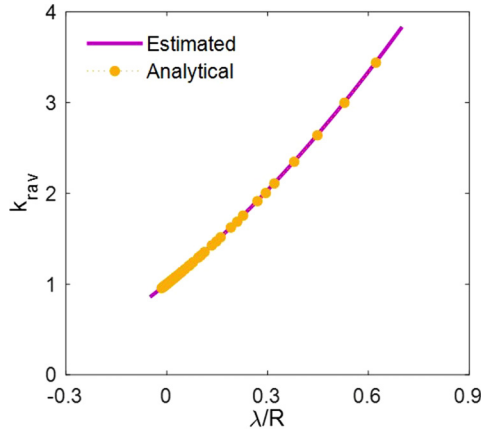


FIG. 6. Comparison of estimated and analytical volumetric PERs as a function of the normalized ASL.

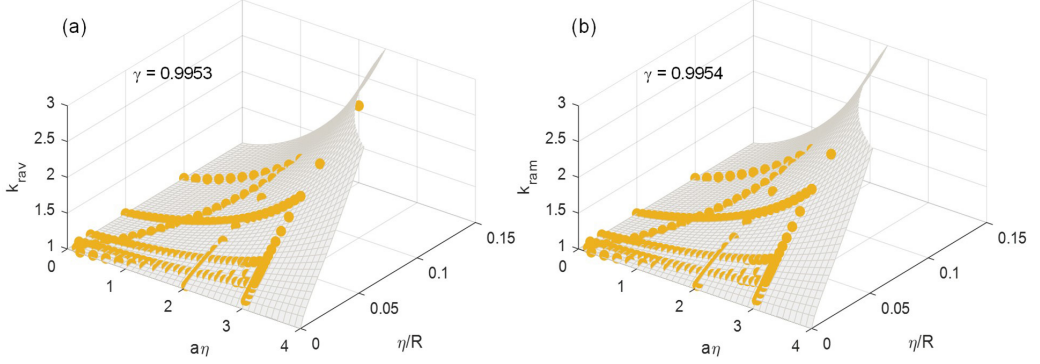


FIG. 7. Volumetric PER (a) and mass PER (b) as a function of the two dimensionless numbers. The circles show the analytical results, while the surfaces represent the fitted results. The value of Pearson correlation coefficient γ is provided in each panel to illustrate the quality of surface fitting.

the flow channel can affect PER; if θ_1 or θ_2 is zero, the corresponding dimensionless number would play a negligible role. Note that the fluid slip ($k_{ra} > 1$) is the focus of investigation here.

In addition to the curves in Figs. 5(a) and 5(b), another four curves within the attainable range of (a, η) are calculated from Eqs. (D4) and (D5). Based on these analytical results, the fitted surface using the relationship in Eq. (16) can be obtained with a fairly good fitting quality, as shown in Fig. 7. Table II provides the fitted coefficients. Within the given range of dimensionless numbers, the relationships between PERs and dimensionless numbers can be described by a simple formulation.

It is interesting that $\theta_2/\theta_1 \approx 0.5$ can be observed in Table II for the proposed FSI force function, indicating that a roughly stable relationship between the effect of the complex FSI strength on PER and that of the gap size may exist. Therefore, a pair of dimensionless numbers $(a\eta, \eta/R)$ for the proposed FSI force functions can be unified into a single dimensionless number, such as $a\eta^{1.5}/R^{0.5}$. The PER can be uniquely determined by the dimensionless number, which serves as an indicator of the key feature of the slip-flow system.

C. Modeling of benchmark slip-flow experiments in planar channels

1. Flow channel with two walls of symmetric FSI properties

A benchmark slip-flow experiment [8] was conducted in a rectangular duct [see Fig. 8(a)]. The length, width, and depth are aligned with the x , y , and z coordinates, and the dimensions are $8.25 \text{ cm} \times 300 \text{ } \mu\text{m} \times 30 \text{ } \mu\text{m}$. While the bare glass surface is hydrophilic, it becomes hydrophobic with a contact angle of 120° when coated with an octadecyltrichlorosilane (OTS) layer of 2.3 nm thickness. The de-ionized water is injected into the microchannel at a constant flow rate by using a syringe pump. The velocity profile, measured at $z = 15 \text{ } \mu\text{m}$ from the solid surface by using micron particle image velocimetry (μ -PIV), was used to validate the mesoscopic LBM model based on the particle-level FSI force function [31], which differs from the FSI force function between fluid particles and the flat wall proposed in this study. Given that the aspect ratio of the cross section of the flow channel is $300 \text{ } \mu\text{m} : 30 \text{ } \mu\text{m} = 10 : 1$, the velocity profile at $y = 150 \text{ } \mu\text{m}$ across the gap

TABLE II. Coefficients for fitted PER as formulated in Eq. (16).

Cases	θ_0	θ_1	θ_2	θ_2/θ_1
k_{rav}	1.1197	1.4215	0.6840	0.4812
k_{ram}	1.3644	1.2995	0.6846	0.5268

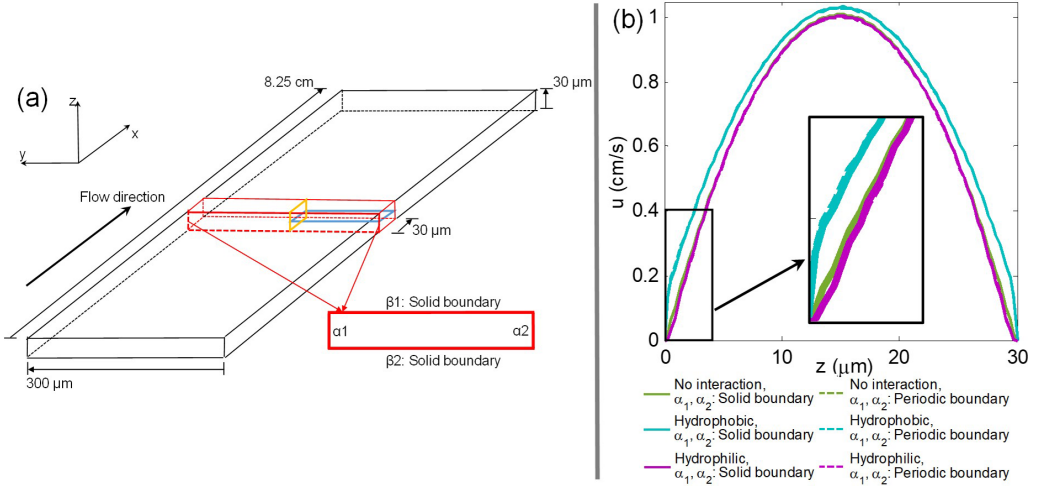


FIG. 8. (a) Dimensions of rectangular duct in slip-flow experiment of Ref. [8] (black lines) and in LBM simulation of Ref. [31] (red lines), respectively. The blue rectangle ($z = 15 \mu\text{m}$) and yellow rectangle ($y = 150 \mu\text{m}$) show the windows of view in the benchmark work and in this study, respectively. The red rectangle shows the cross section of the microchannel. The top and bottom walls, β_1 and β_2 , are solid boundaries (where the no-slip boundary condition and the FSI force are both applied), and the left and right walls, α_1 and α_2 , can be solid or periodic boundaries in the LBM simulation. The solid walls (α_1 , α_2 , β_1 , and β_2) are uniformly hydrophilic or hydrophobic. (b) Comparison of the simulated velocity profiles using the validated LBM model [31] when α_1 and α_2 are solid and periodic boundaries, respectively.

of our interest is controlled by the top and bottom walls (β_1 and β_2). Unfortunately, this velocity profile was not measured in the flow experiment of Ref. [8]. We have to acquire it from the numerical simulations using the validated LBM model in Ref. [31].

Prior to this, we should check if the analytical solutions (for two parallel walls) proposed in this work are applicable to the rectangular duct (with four solid walls) used in the flow experiment [8]. The walls β_1 and β_2 are designated solid boundaries, whereas the walls α_1 and α_2 can be eliminated by being implemented as periodic boundaries in the LBM simulation. Figure 8(b) shows that the simulated velocity profiles for hydrophilic, hydrophobic, and no-interaction solid surfaces are almost the same regardless of whether α_1 and α_2 are solid boundaries or periodic boundaries. These results show that the effect of the left and right walls (α_1 and α_2) on the velocity profile of our interest is negligible, and the rectangular duct in the flow experiment can be simplified as a parallel-plate channel. Thus, the exact solutions in Eqs. (B3), (B5), and (C7) for the two walls of symmetric FSI properties can be applied in this case.

In our analytical method, the rule of unit conversion is regulated as follows: $2R = 600 \text{ lu}$, $\nu = 3.0 \text{ lu}^2/\text{ts}$, and $\rho_0 = 1.0 \text{ mu}/\text{lu}^3$ (where mu is the mass unit in the LBM model framework) are used to represent the size of the gap of the flow channel ($30 \mu\text{m}$), the kinematic viscosity of water ($1.5 \times 10^{-6} \text{ m}^2/\text{s}$), and the density of water ($1.0 \times 10^3 \text{ kg}/\text{m}^3$), respectively. As illustrated in Fig. 9(a), the FSI parameters (a , η) can be acquired by fitting to the simulated velocity profile using our analytical solution. With the two fitted parameters, the ASL is calculated to be $1.16 \mu\text{m}$ for the hydrophobic surface, which is consistent with the slip length of $1.0 \pm 0.45 \mu\text{m}$ as estimated in Ref. [8]. That the measured and calculated ASLs for this flow cell are much larger than those (less than tens of nanometers) observed in surface force apparatus experiments [17,18] can be attributed to the following reality: Some microbubbles may be coated or trapped on the rough hydrophobic surface providing a highly less viscous layer to the bulk water flow. It is indicated that the proposed model framework may provide an artificial but effective approach of introducing a lower interfacial resistance. For the hydrophilic surface, the ASL is calculated as $-0.37 \mu\text{m}$, where the multilayer

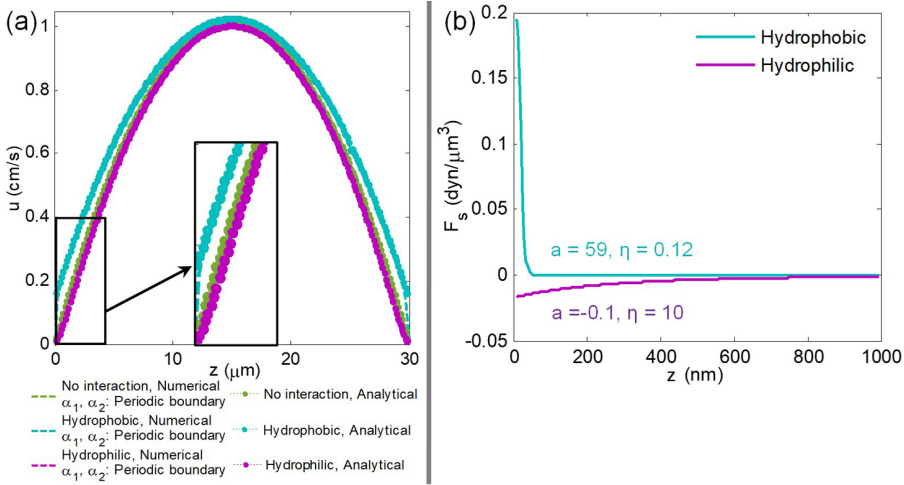


FIG. 9. (a) Comparison of numerical velocity profile (obtained from the validated LBM model [31]) and analytical velocity profile (for recovering FSI parameters). (b) Recovered FSI force curves for hydrophilic and hydrophobic surfaces.

sticking was noticed but not quantified in the simulation work of Ref. [33]. Figure 9(b) shows the recovered force curves with the density profile included.

2. Flow channel with two walls of asymmetric FSI properties

Another slip-flow experiment [9] with an improved measurement accuracy which can observe the slip length below 100 nm was carried out in a similar rectangular duct [see Fig. 8(a)]. The depth of the microchannel is $12.7 \mu\text{m}$ as indicated by the range of the measured velocity profile, and the length and width are 1.0 cm and $100 \mu\text{m}$, respectively. The top boundary ($z = 12.7 \mu\text{m}$) is made of polydimethylsiloxane (PDMS) using a standard soft lithography technique, while the bottom wall can be a hydrophilic bare glass, or a hydrophobic glass coated with monolayers of OTS on which the contact angle of de-ionized water is 95° . In this section, only the slip-flow effect on the glass wall or OTS wall at the bottom is the focus of our interest. The flow rate is controlled by the specified pressure drop. The velocity measurement is made by the μ -PIV system, where the dimension of the window of view on the x - y plane is $12 \mu\text{m} \times 25 \mu\text{m}$, and the scan is realized on the z axis with a step increment of 50 nm in order to measure the velocity profile across the channel. The wall location can be determined within an uncertainty of 30 nm which is much lower than that in the observation system in Ref. [8]. The aspect ratio of the flow channel is as large as $100 \mu\text{m} : 12.7 \mu\text{m} = 7.87 : 1$, and so the rectangular duct can be considered as a parallel-plate channel in terms of the velocity profile across the channel.

A general parabolic function is used to fit the observed velocity profiles [see Fig. 10(a)] for the glass-PDMS and OTS-PDMS microchannels. Then the ASLs for glass wall and OTS wall can be determined to be 38.0 and -58.3 nm, respectively, which are consistent with the reported values of slip lengths [9], 50.0 ± 50.0 nm, and -35.0 ± 100.0 nm. Considering that the two walls of the microchannel in this slip-flow experiment are made of different materials, our exact solutions are not applicable. The numerical solutions as formulated in Eqs. (6)–(9) for the case of asymmetric FSI properties are therefore employed here to fit the observed velocity profiles. By using the same rule of conversion between physical and lattice units as that used in the previous section, the FSI parameters (a_1, η_1) for glass wall and OTS wall and (a_2, η_2) for PDMS wall can be recovered [see Fig. 10(b)], respectively.

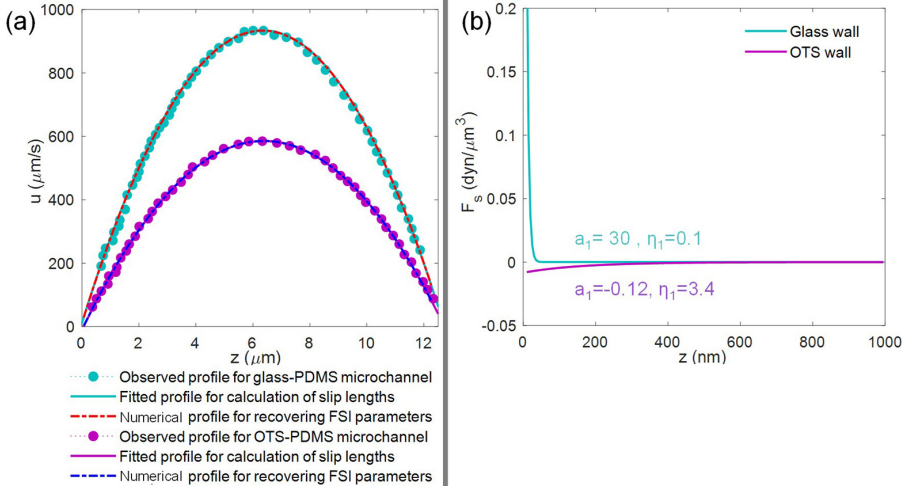


FIG. 10. (a) Comparison of observed velocity profile extracted from Ref. [9], fitted velocity profile for slip length determination, and numerical velocity profile for FSI parameter estimation. The fitted parabolic functions are $u(z) = -22.961 z^2 + 291.191z + 11.099$ and $u(z) = -14.596 z^2 + 186.560z - 10.822$ for glass-PDMS and OTS-PDMS microchannels, respectively, and the average ASL for PDMS wall is 21.6 nm. (b) Recovered FSI force curves with (a_1, η_1) for glass and OTS walls, respectively. Estimated FSI parameters for PDMS wall are $(a_2, \eta_2) = (6.0, 0.2)$.

3. Discussions on the observed and simulated results of the two slip-flow experiments

The μ -PIV observation system is used in the slip-flow experiments [8,9] to measure the velocity profile, where there is an inherent issue of wall location determination that reduces the accuracy of velocity measurement near a solid surface. The fluorescent beads (flow tracer) as large as a diameter of larger than 100 nm can be absorbed by the wall, and their trajectory within approximately three particle radii cannot accurately represent those of the fluid. We can see that the uncertainties (50–100 nm) in slip length measurement in Ref. [9] is significantly less than 450 nm in Ref. [8], but they are still comparable to the mean values of slip length, which should be further reduced for accurate analysis of the chemical properties of the microchannel boundary.

The observed and simulated results of the slip flow of de-ionized water at the surface of five types of solid walls [8,9] are summarized in Table III. The affinity of water molecules to a solid wall depends on how firmly the functional groups on the solid surface can bond with water. The glass composed of fused silica is of high surface free energy and is naturally hydrophilic (cases A and D). Usually the no-slip boundary condition can be satisfied on the hydrophilic wall. However, a negative value of ASL is obtained in case A implying multilayer sticking, and fluid slip is surprisingly observed in case D. OTS layers and PDMS materials, which prevent the hydroxyl groups on the silica surface from bonding with water molecules, can make the solid wall hydrophobic (cases B, C, and E). Fluid slip is naturally observed in cases B and C, but multilayer sticking is measured in case E. We can see that the fluid flow can slip on hydrophobic surfaces (cases B and C) as predicted by the formula [21], $\lambda = C/(1 + \cos\theta)^2$ (where λ , θ , and C are slip length, contact angle, and fitted constant, respectively). Also, the stronger hydrophobicity as characterized by a larger contact angle results in a larger slip length in case B than that in case C. The other reason for this may be due to the shear rate effect [18] because the shear rate in case B is estimated to be approximately 4.58 times as large as that in case C.

However, the consistency of the predictions by the formula [21] with observations did not hold for all the cases. For example, the formula does not recognize the negative slip length for a hydrophilic surface (case A), and cannot explain why fluid slip occurs on a hydrophilic surface (case D) and

TABLE III. Summary of the observed and simulated results of the two slip-flow experiments.

	Slip-flow experiment in Ref. [8]		Slip-flow experiment in Ref. [9]	
	Case A	Case B	Case C	Case E
Flowing fluid	De-ionized water	De-ionized water	De-ionized water	De-ionized water
Solid wall	Bare glass (hydrophilic)	Glass with OTS layer (hydrophobic)	PDMS wall (hydrophobic)	Bare glass (hydrophilic) / Glass with OTS layer (hydrophobic)
Contact angle	–	120°	105°	95°
Channel depth	30 μm	30 μm	12.7 μm	12.7 μm
Observed slip length λ	–	1.0 \pm 0.45 μm	21.6 \pm 50.0 nm	50.0 \pm 50.0 nm
Simulated slip length λ	–0.37 μm	1.16 μm	21.6 nm	38.0 nm
Fitted interaction parameters (a, η)	(–0.1, 10)	(59, 0.12)	(6.0, 0.2)	(30, 0.1)
Dimensionless number $a\eta^{1.5}/R^{0.5}$	–0.183	0.1416	0.0476	0.0842
Simulated density ratio ρ_{ra}	2.47	0.998	0.992	0.999

multilayer sticking takes place on a hydrophobic surface (case E). In case A, the hydrophilicity of the bare glass can be affected by the surface cleanness and impurity [49]. If it is sufficiently clean that more hydroxyl groups are exposed to the flowing water, multilayers of water molecules can stick to the glass surface [22] to form a condensed water layer as characterized by the density larger than that of free water [42–44]. In case D, coupled with water-surface interaction, the water molecule distribution within the contact layer should be taken into consideration [15]. If water molecules migrate from one adsorption site to the neighboring sites within the contact layer, liquid slip can occur irrespectively of the contact angle. In case E, the contact angle of 95° suggests that the surface tends to be a neutral one. However, the measurement of contact angle, due to the hysteresis effect, can be affected by a few factors [49], such as static or dynamic condition, rate of liquid movement, surface roughness and heterogeneity, and droplet volume. Moreover, the measurement error of 100 nm larger than the mean value of slip length cannot ensure whether fluid slips or sticks on the solid surface. All of these inconsistencies with the prediction of slip length from contact angle [21], due to difficulties in contact angle measurement and neglect of water molecule distribution in the film layer, suggest that contact angle alone is not a reliable variable for descriptions of hydrophobicity of the solid surface on which the fluid flows.

The fitted FSI parameters of our proposed model show a better consistency with the observed slip length than contact angle. For example, with the fitted η (of almost the same values in cases B and D), a larger value of a leads to larger slip length in case B than those in case D. Similar agreement is evident for cases A and E. In all cases, the value of the dimensionless number, $a\eta^{1.5}/R^{0.5}$, proposed in Sec. III B, is positively correlated with the magnitude of slip length for $a > 0$ and $a < 0$, respectively, and can serve as a unique indicator of the slip flow on the specified solid surface. The recovered force curves exhibit similar shapes in the two flow experiments [8,9]: The repulsive FSI force for fluid slip has a short range (up to 20–50 nm) but a higher strength, while the attractive FSI force for multilayer sticking has a longer distance (up to 300–400 nm) but a weaker strength [see Figs. 9(b) and 10(b)]. The significance of the recovered FSI force curve lies in that it can be used to predict the slip flow for the given fluid-solid interface for various sizes of the flow channel. The calculated density ratios in all cases are roughly within the observed range [see Fig. 3]. Nonetheless, the simulated near-wall density profile obtained from the fitted interaction parameters still cannot be verified due to the lack of experimental data.

IV. CONCLUSIONS

This paper proposes an exponentially decaying force function to describe the physics of the FSI force in the LBM model framework, which is responsible for apparent liquid slip flow ($0.001 < \text{Kn} < 0.1$) between two confined parallel plates. Beyond the work of Benzi *et al.* [27,28], exact solutions are derived by using the pressure equation accounting for the symmetric mesoscale FSI process of the two walls. The exact solutions for density profile, velocity profile, and PER, and the asymptotic solution for ASL, explicitly relate the macroscale flow properties to the mesoscale FSI parameters and the size of the gap of the flow channel. They are numerically solvable by using MATLAB and are validated by the LBM solutions. The dimensionless numbers $[g_s\eta/(R_gT), \eta/R]$ are also derived for the slip-flow system.

The FSI parameters cannot take arbitrary values. The physically consistent range is provided based on the observed range of density ratio ($0.1 < \rho_{ra} < 2.0$). The behavior of film and bulk fluid density profiles and near-wall and bulk flow velocity profiles stems from the intrinsic decay form of the proposed FSI force function. Within the attainable range of dimensionless numbers, a simple relationship between PERs and dimensionless numbers can be obtained by fitting. It is found that the two dimensionless numbers can be combined into a single one, $g_s\eta^{1.5}/(R^{0.5}R_gT)$, indicating the existence of a stable relationship between the effect of the complex FSI strength on PER and that of the gap size. The exact solutions contribute to formulating the water slip flow in microfluidic devices and tight porous media and provide some useful insights in the engineering context.

We also apply our proposed model to two benchmark flow experiments [8,9]. The continuous FSI force with two free parameters was successfully calibrated by fitting to the simulated velocity profile [8] using the exact solution for the symmetric FSI forces, or by fitting to the observed velocity profile [9] using the numerical solution for the walls of asymmetric FSI property. In future work, we will further demonstrate the validity of the proposed FSI force model in the other types of slip-flow microchannel, such as Couette flow in a planar channel, and Poiseuille flow in a cylindrical tube, etc., where accurate measurements of slip length and near-wall density profile are available.

ACKNOWLEDGMENTS

This work was funded by China Postdoctoral Science Foundation (Grant No. 2020M680081). The authors also acknowledge the financial support from Westlake Institute for Advanced Study, Westlake University and The University of Queensland, and appreciate the computational capacity of High-Performance Computing Cluster of The University of Queensland.

APPENDIX A: FLUID PRESSURE CONSIDERING FSI FORCE

In order to describe the mechanical balance near the solid surface, we have to link the proposed FSI force equation in Eq. (4) with the formula of fluid pressure (p) by requiring at every lattice node that [50,51]

$$\nabla p = -\mathbf{F}_s, \quad (\text{A1})$$

which suggests that the fluid pressure everywhere within the gap is a constant when the slip flow reaches the steady state. On the other hand, in the light of invariance of the longitudinal profiles of density and velocity, we describe the one-dimensional profile only in the y direction. Thus, starting from Eq. (A1), we can reformulate it by executing an integral calculation over the interval $y_0 \rightarrow y$ on both sides, as follows,

$$p(y) - p_0 = - \int_{y_0}^y \mathbf{F}_s(s) ds, \quad (\text{A2})$$

where the bulk fluid pressure at $y = y_0$ [due to the total FSI force $\mathbf{F}_s(y_0) = 0$] is $p_0 = \rho R_g T$ [47] under the ideal gas condition as assumed in this work. Then rearrangement of Eq. (A2) gives rise to the fluid pressure equation considering the FSI force (for the film and bulk fluids), as in the following [27,28]:

$$p(y) = \rho(y) R_g T - \int_{y_0}^y \mathbf{F}_s(s) ds. \quad (\text{A3})$$

APPENDIX B: DENSITY AND VELOCITY PROFILES

Replacing the fluid pressure term in Eq. (11) by Eq. (5), which considers the mesoscale FSI force, gives

$$\partial_y \rho - \frac{g_s}{R_g T} \rho(y) \left[\exp\left(-\frac{y}{\eta}\right) - \exp\left(-\frac{2R-y}{\eta}\right) \right] = 0. \quad (\text{B1})$$

Set $a = g_s/(R_g T)$, which refers to the interaction strength in the following unless stated otherwise. Equation (B1) can be rewritten as

$$\frac{\partial_y \rho}{\rho(y)} = a \left[\exp\left(-\frac{y}{\eta}\right) - \exp\left(-\frac{2R-y}{\eta}\right) \right]. \quad (\text{B2})$$

By solving the homogeneous ordinary differential equation (B2) for the fluid density with the aid of the auxiliary condition (13), the analytical solution for the density profile can be formulated as

$$\rho(y) = \rho_0 A \exp[-a\eta w(y)], \quad (\text{B3})$$

where

$$w(y) = \left[\exp\left(-\frac{y}{\eta}\right) + \exp\left(-\frac{2R-y}{\eta}\right) \right] (0 < y < 2R), \quad A = \frac{R}{\int_0^R \exp[-a\eta w(y)] dy}.$$

By rearranging Eq. (12), we obtain

$$\partial_y^2 u + \frac{\partial_y \rho}{\rho(y)} \partial_y u = -\frac{g}{\nu}. \quad (\text{B4})$$

Specify $b = g/\nu$ which describes the magnitude of the external body force in the following unless stated otherwise. Equation (B4) is an inhomogeneous ordinary differential equation for the flow velocity. By applying the condition (14), the analytical solution for the velocity profile is solved as

$$u(y) = b \int_0^y \int_r^R \exp\{a\eta[w(r) - w(s)]\} ds dr. \quad (\text{B5})$$

APPENDIX C: ASL AND PER

Equation (B5) should be transformed into the same form as Eq. (2) for the bulk velocity profile in order to acquire the ASL. We reformulate the velocity profiles for the proposed FSI force functions as

$$u(y) = \frac{b}{2} q(y), \quad (\text{C1})$$

where

$$q(y) = 2 \int_0^y \int_r^R \exp\{a\eta[w(r) - w(s)]\} ds dr.$$

The expression for $q(y)$ can be approximated by a second-order Taylor series expansion around the middle of the gap ($y \approx R$). Then Eq. (C1) may be rearranged as

$$u(y)|_{y \approx R} \cong \frac{b}{2} \left[\frac{q(R)}{0!} + \frac{\partial_y [q(R)]}{1!} (y - R) + \frac{\partial_y^2 [q(R)]}{2!} (y - R)^2 \right]. \quad (\text{C2})$$

The function $q(x)$ and its derivatives at $x = R$ are

$$q(R) = q(R), \quad \partial_y [q(R)] = 0, \quad \partial_y^2 [q(R)] = -2. \quad (\text{C3})$$

Substituting the computed Taylor coefficients into Eq. (C2) produces

$$u(y)|_{y \approx R} \cong \frac{b}{2} [-y^2 + 2Ry + q(R) - R^2]. \quad (\text{C4})$$

Although Eq. (C4) approximates Eq. (C1) only at $y \approx R$, it can represent the whole bulk velocity profile equivalent to Eq. (2), because the bulk velocity profile in the presence of FSI force retains the Poiseuille-flow nature and the same kinematic viscosity [31]. By comparing Eq. (C4) with Eq. (2), we can obtain a parabolic equation with the unknown ASL:

$$\lambda^2 + 2R\lambda + R^2 - q(R) = 0. \quad (\text{C5})$$

In this sense, the obtained expression of ASL (normalized by the gap between the two flat walls) is an asymptotic solution, as presented below:

$$\frac{\lambda}{R} = \frac{1}{R} \sqrt{q(R)} - 1. \quad (\text{C6})$$

Substituting the expression for $q(R)$ into Eq. (C6) gives the normalized ASL (evaluating how much the slip-flow affects the macroscopic flow),

$$\frac{\lambda}{R} = \frac{1}{R} \sqrt{2 \int_0^R \int_r^R \exp\{a\eta[w(r) - w(s)]\} ds dr} - 1. \quad (\text{C7})$$

The volumetric flux (Q_v) or mass flux (Q_m) can be calculated based on the velocity and density profiles, *namely*, $Q_v = \int_0^R u(y) dy$, $Q_m = \int_0^R \rho(y) u(y) dy$. Then volumetric PER (k_{rav}) and the mass PER (k_{ram}) can be given by

$$k_{rav} = \frac{3}{R^3} \int_0^R \int_0^y \int_r^R \exp\{a\eta[w(r) - w(s)]\} ds dr dy, \quad (\text{C8})$$

$$k_{ram} = \frac{3A}{R^3} \int_0^R \int_0^y \int_r^R \exp\{a\eta[-w(y) + w(r) - w(s)]\} ds dr dy. \quad (\text{C9})$$

APPENDIX D: DIMENSIONLESS NUMBERS

The exact solutions in Eqs. (B3), (B5), and (C7)–(C9) can be nondimensionalized by defining

$$\rho' = \frac{\rho}{\rho_0}, \quad u' = \frac{2u}{bR^2}, \quad y' = \frac{y}{R}, \quad r' = \frac{r}{R}, \quad s' = \frac{s}{R}.$$

Then the density and velocity profiles can be rewritten in a nondimensional form,

$$\rho'(y') = A \exp[-a\eta w(y')], \quad (\text{D1})$$

$$u'(y') = 2 \int_0^{y'} \int_{r'}^1 \exp\{a\eta[w(r') - w(s')]\} ds' dr', \quad (\text{D2})$$

where

$$w(y') = \exp\left(-\frac{y'}{\eta/R}\right) + \exp\left(-\frac{2-y'}{\eta/R}\right) (0 < y' < 2), \quad A = \frac{1}{\int_0^1 \exp[-a\eta w(y')] dy'}$$

The same nondimensionalization can also be made for the normalized ASL and the volumetric and mass PERs, which take the form

$$\frac{\lambda}{R} = \sqrt{2 \int_0^1 \int_{r'}^1 \exp\{a\eta[w(r') - w(s')]\} ds' dr'} - 1, \quad (\text{D3})$$

$$k_{rav} = 3 \int_0^1 \int_0^{y'} \int_{r'}^1 \exp\{a\eta[w(r') - w(s')]\} ds' dr' dy', \quad (\text{D4})$$

$$k_{ram} = 3A \int_0^1 \int_0^{y'} \int_{r'}^1 \exp\{a\eta[-w(y') + w(r') - w(s')]\} ds' dr' dy'. \quad (\text{D5})$$

We can see that the nondimensional $w(y')$ is a function of a ratio of length scale to length scale, η/R . The inclusion of $w(y')$ into the right-hand side of Eqs. (D1)–(D5) leads to a new term, $a\eta$. For the proposed FSI force function, $a\eta = g_s \eta / (R_g T)$ is a ratio of square of velocity to square

of velocity. Therefore, $[g_s\eta/(R_gT), \eta/R]$ can be considered as the dimensionless numbers for the slip-flow system of investigation based on the proposed FSI force function.

-
- [1] L. Bocquet and E. Charlaix, Nanofluidics: From bulk to interfaces, *Chem. Soc. Rev.* **39**, 1073 (2010).
 - [2] S. Roy, R. Raju, H. F. Chuang, B. A. Cruden, and M. Meyyappan, Modeling gas flow through microchannels and nanopores, *J. Appl. Phys.* **93**, 4870 (2003).
 - [3] A. Sakhaee-Pour and S. Bryant, Gas permeability of shale, *SPE Reservoir Eval. Eng.* **15**, 401 (2012).
 - [4] C. Neto, D. R. Evans, E. Bonaccorso, H. J. Butt, and V. S. Craig, Boundary slip in Newtonian liquids: A review of experimental studies, *Rep. Prog. Phys.* **68**, 2859 (2005).
 - [5] J. J. Shu, J. B. M. Teo, and W. K. Chan, Fluid velocity slip and temperature jump at a solid surface, *Appl. Mech. Rev.* **69**, 020801 (2017).
 - [6] E. Schnell, Slippage of water over nonwetttable surfaces, *J. Appl. Phys.* **27**, 1149 (1956).
 - [7] N. V. Churaev, V. D. Sobolev, and A. N. Somov, Slippage of liquids over lyophobic solid surfaces, *J. Colloid Interface Sci.* **97**, 574 (1984).
 - [8] D. C. Tretheway and C. D. Meinhart, Apparent fluid slip at hydrophobic microchannel walls, *Phys. Fluids* **14**, L9 (2002).
 - [9] P. Joseph and P. Tabeling, Direct measurement of the apparent slip length, *Phys. Rev. E* **71**, 035303(R) (2005).
 - [10] D. X. Liu, X. A. Yue, L. M. Wang, J. R. Hou, and J. H. Zhang, Model study on the irreducible water saturation by centrifuge experiments, *J. Pet. Sci. Eng.* **53**, 77 (2006).
 - [11] Q. Zhang, Y. Su, W. Wang, M. Lu, and G. Sheng, Apparent permeability for liquid transport in nanopores of shale reservoirs: Coupling flow enhancement and near-wall flow, *Int. J. Heat Mass Transfer* **115**, 224 (2017).
 - [12] S. Yang, S. M. Dammer, N. Bremond, H. J. Zandvliet, E. S. Kooij, and D. Lohse, Characterization of nanobubbles on hydrophobic surfaces in water, *Langmuir* **23**, 7072 (2007).
 - [13] D. C. Tretheway and C. D. Meinhart, A generating mechanism for apparent fluid slip in hydrophobic microchannels, *Phys. Fluids* **16**, 1509 (2004).
 - [14] M. J. Davis and E. Lauga, Geometric transition in friction for flow over a bubble mattress, *Phys. Fluids* **21**, 011701 (2009).
 - [15] T. A. Ho, D. V. Papavassiliou, L. L. Lee, and A. Striolo, Liquid water can slip on a hydrophilic surface, *Proc. Natl. Acad. Sci. USA* **108**, 16170 (2011).
 - [16] J. N. Israelachvili, *Intermolecular and Surface Forces* (Academic Press, New York, 2011).
 - [17] J. Baudry, E. Charlaix, A. Tonck, and D. Mazuyer, Experimental evidence for a large slip effect at a nonwetting fluid-solid interface, *Langmuir* **17**, 5232 (2001).
 - [18] V. S. J. Craig, C. Neto, and D. R. M. Williams, Shear-Dependent Boundary Slip in an Aqueous Newtonian Liquid, *Phys. Rev. Lett.* **87**, 054504 (2001).
 - [19] O. I. Vinogradova, Implications of hydrophobic slippage for the dynamic measurements of hydrophobic forces, *Langmuir* **14**, 2827 (1998).
 - [20] O. I. Vinogradova, Slippage of water over hydrophobic surfaces, *Int. J. Miner. Process.* **56**, 31 (1999).
 - [21] D. M. Huang, C. Sendner, D. Horinek, R. R. Netz, and L. Bocquet, Water Slippage versus Contact Angle: A Quasiuniversal Relationship, *Phys. Rev. Lett.* **101**, 226101 (2008).
 - [22] K. Wu, Z. Chen, J. Li, X. Li, J. Xu, and X. Dong, Wettability effect on nanoconfined water flow, *Proc. Natl. Acad. Sci. USA* **114**, 3358 (2017).
 - [23] J. Harting, C. Kunert, and H. J. Herrmann, Lattice Boltzmann simulations of apparent slip in hydrophobic microchannels, *Europhys. Lett.* **75**, 328 (2006).
 - [24] C. Kunert and J. Harting, On the effect of surfactant adsorption and viscosity change on apparent slip in hydrophobic microchannels, *Prog. Comput. Fluid Dyn.* **8**, 018090 (2008).
 - [25] J. Zhang and D. Y. Kwok, Apparent slip over a solid-liquid interface with a no-slip boundary condition, *Phys. Rev. E* **70**, 056701 (2004).

- [26] J. Zhang, B. Li, and D. Y. Kwok, Mean-field free-energy approach to the lattice Boltzmann method for liquid-vapor and solid-fluid interfaces, *Phys. Rev. E* **69**, 032602 (2004).
- [27] R. Benzi, L. Biferale, M. Sbragaglia, S. Succi, and F. Toschi, Mesoscopic two-phase model for describing apparent slip in micro-channel flows, *Europhys. Lett.* **74**, 651 (2006).
- [28] R. Benzi, L. Biferale, M. Sbragaglia, S. Succi, and F. Toschi, Mesoscopic modeling of a two-phase flow in the presence of boundaries: The contact angle, *Phys. Rev. E* **74**, 021509 (2006).
- [29] A. Montessori, C. A. Amadei, G. Falcucci, M. Sega, C. D. Vecitis, and S. Succi, Extended friction elucidates the breakdown of fast water transport in graphene oxide Membranes, *Europhys. Lett.* **116**, 54002 (2006).
- [30] C. A. Amadei, A. Montessori, J. P. Kadow, S. Succi, and C. D. Vecitis, Role of oxygen functionalities in graphene oxide architectural laminate subnanometer spacing and water transport, *Environ. Sci. Technol.* **51**, 4280 (2017).
- [31] Z. Li, S. Galindo-Torres, A. Scheuermann, and L. Li, Mesoscopic approach to fluid-solid interaction: Apparent liquid slippage and its effect on permeability estimation, *Phys. Rev. E* **98**, 052803 (2018).
- [32] S. Succi, Mesoscopic Modeling of Slip Motion at Fluid-Solid Interfaces with Heterogeneous Catalysis, *Phys. Rev. Lett.* **89**, 064502 (2002).
- [33] L. Zhu, D. Tretheway, L. Petzold, and C. Meinhart, Simulation of fluid slip at 3D hydrophobic microchannel walls by the lattice Boltzmann method, *J. Comput. Phys.* **202**, 181 (2005).
- [34] G. H. Tang, W. Q. Tao, and Y. L. He, Lattice Boltzmann method for gaseous microflows using kinetic theory boundary conditions, *Phys. Fluids* **17**, 058101 (2005).
- [35] G. H. Tang, W. Q. Tao, and Y. L. He, Lattice Boltzmann method for simulating gas flow in microchannels, *Int. J. Mod. Phys. C* **15**, 335 (2004).
- [36] M. Sbragaglia and S. Succi, Analytical calculation of slip flow in lattice Boltzmann models with kinetic boundary conditions, *Phys. Fluids* **17**, 093602 (2005).
- [37] R. Benzi, L. Biferale, M. Sbragaglia, S. Succi, and F. Toschi, Mesoscopic modelling of heterogeneous boundary conditions for microchannel flows, *J. Fluid Mech.* **548**, 257 (2006).
- [38] Z. Li, S. Galindo-Torres, G. Yan, A. Scheuermann, and L. Li, A lattice Boltzmann investigation of steady-state fluid distribution, capillary pressure and relative permeability of a porous medium: Effects of fluid and geometrical properties, *Adv. Water Resour.* **116**, 153 (2018).
- [39] Z. Li, S. Galindo-Torres, G. Yan, A. Scheuermann, and L. Li, Pore-scale simulations of simultaneous steady-state two-phase flow dynamics using the lattice Boltzmann model: Interfacial area, capillary pressure and relative permeability, *Transp. Porous Media* **129**, 295 (2019).
- [40] N. Lu and W. J. Likos, *Unsaturated Soil Mechanics* (John Wiley & Sons, New York, 2004).
- [41] D. M. Anderson and P. F. Low, Density of water adsorbed on Wyoming bentonite, *Nature* **180**, 1194 (1957).
- [42] R. T. Martin, Adsorbed water on clay: A review, in *Clays and Clay Minerals: Proceedings of the Ninth National Conference* (Pergamon Press, Oxford, 1962), p. 28.
- [43] P. P. Olodovskii, Adsorbed water density distribution in disperse media, *J. Eng. Phys.* **12**, 263 (1967).
- [44] P. P. Olodovskii, Density of adsorbed water in disperse systems, *J. Eng. Phys.* **40**, 433 (1981).
- [45] D. T. Ewing and C. H. Spurway, The density of water adsorbed on silica gel, *J. Am. Chem. Soc.* **52**, 4635 (1930).
- [46] K. Kulasinski, Effects of water adsorption in hydrophilic polymers, in *Polymer Science: Research Advances, Practical Applications and Educational Aspects*, edited by A. M. Vilas and A. S. Martin (Formatex Research Center, Norristown, PA, 2016), p. 217.
- [47] S. Succi, *The Lattice Boltzmann Equation: For Fluid Dynamics and Beyond* (Oxford University Press, Oxford, 2001).
- [48] M. L. Porter, E. T. Coon, Q. Kang, J. D. Moulton, and J. W. Carey, Multicomponent interparticle-potential lattice Boltzmann model for fluids with large viscosity ratios, *Phys. Rev. E* **86**, 036701 (2012).

- [49] J. Drelich, E. Chibowski, D. D. Meng, and K. Terpilowski, Hydrophilic and superhydrophilic surfaces and materials, [Soft Matter](#) **7**, 9804 (2011).
- [50] M. Sbragaglia and X. Shan, Consistent pseudopotential interactions in lattice Boltzmann models, [Phys. Rev. E](#) **84**, 036703 (2011).
- [51] C. S. From, E. Sauret, S. A. Galindo-Torres, and Y. T. Gu, Interaction pressure tensor on high-order lattice Boltzmann models for nonideal fluids, [Phys. Rev. E](#) **99**, 063318 (2019).